

Morphological evaluation of hard tissues irradiated by holmium laser under various environments using optical coherence microscopy

Tao Lü · Qing Xiao

Received: 22 February 2012 / Revised: 11 May 2012 / Published online: 16 September 2012
© Springer-Verlag 2012

Abstract In order to investigate the influence of water environment on fiber-guided holmium laser ablation of hard tissues, high-speed photography is performed to accurately record the dynamic evolutions of vaporization bubbles and ablation plumes, and optical coherence microscopy is also used to measure the crater morphology. Experimental results indicate that under the same condition, the ablation performances in air and in water for a single long-pulse laser are comparable when the used fibers are in perpendicular contact with the tissues. But for multiple-pulses ablation, the ablation performances such as ablation efficiency and surface morphology in water become better than those in air because of more and more significant vaporization effect for bigger ablation craters. Optical coherence microscopy is an effective tool for the morphological measurement of craters.

1 Introduction

Enhancement of laser ablation in the presence of a liquid layer has been of interest in various technical and medical

areas such as surface cleaning [1, 2], particle removal [3], material processing [4–6], laser osteotomy [7], and dental tissue ablation [8, 9]. The improved ablation speed, ablation efficiency, surface morphology, etc., with a liquid-assisted ablation, are associated with explosive vaporization effect (VE) for long-pulse durations and confinement of plasma expansion for short-pulse durations [10, 11]. Unlike short-pulse laser ablation [6, 9, 12, 13], free-running long-pulse laser ablation is more complicated in that plume formation and expansion occurs largely during the laser irradiation. The ablation plumes (AP) influence the energy deposition of the laser radiation into the tissue, and the plume dynamics itself is also influenced by the interaction of the laser beam with the ejected material [14, 15]. Therefore, analysis of AP and crater morphology induced by long-pulse lasers is crucial to determine the ablation difference under various environments.

Conventionally, crater measurement using histological methods, scanning electron microscopy, atomic force microscopy, X-ray computed tomography, and optical coherence tomography (OCT) has been performed to quantitatively measure the morphologies of craters irradiated by pulsed lasers [16]. The histological methods require the sample to be cut into serial sections and then imaged by microscopy. This is a destructive process and the possibility of damage during the cutting process cannot be excluded. In the case of scanning electron microscopy, samples need to be coated with a thin film of conducting material [17]. Atomic force microscopy has a limited range of scanning and is thus only suited to small samples with size of the order of hundreds of microns [18]. X-ray computed tomography is a non-contact and non-preprocessing method, but it requires a longer time to implement and has less resolution of approximately tens of microns [19]. In contrast, OCT is a potential tool for monitoring the

T. Lü (✉)
School of Mathematics and Physics, China University
of Geosciences, Wuhan 430074, China
e-mail: lvtaohn@126.com

T. Lü
Medical Laser Center Lübeck GmbH, Peter-Monnik-Weg 4,
23562 Lübeck, Germany

Q. Xiao (✉)
Britton Chance Center for Biomedical Photonics,
Wuhan National Laboratory for Optoelectrics, Huazhong
University of Science and Technology, Wuhan 430074, China
e-mail: sophierxq@gmail.com

variation in the geometrical shape of the crater with non-contact, high-speed, and non-preprocessing advantages. OCT usually has resolution of approximately a dozen microns and a measurement range of up to several millimeters. However, imaging technique with higher resolution is necessary to observe the fine structure and small variation. For example, the measurement range for the tissue induced by one laser pulse is entirely several tens of microns or less. Though the principle of optical coherence microscopy (OCM) is similar to OCT in using interferometry scheme and wide-band light source to acquire tomographic images, full-field OCM is a technique that can obtain 3D structure with much higher resolution of $\sim 1 \mu\text{m}$.

In this paper, we present a full-field OCM system, which can measure quantitatively the morphologies of laser-induced craters, to clarify the ablation differences for long-pulse-laser ablation in air and in water.

2 Full-field optical coherence microscopy (OCM)

A schematic diagram of the full-field OCM system used in this experiment is shown in Fig. 1. The system employs a tungsten halogen light source with output power of 10 mW. The light is collimated by an achromatic lens and split into reference and sample beams by a beam splitter that is coated for the visible wavelength range. Two neutral-density filters are added to the reference beam and the sample beam, respectively, to match the back-scattering intensity and to compensate for dispersion. Light is then converged by a pair of $10\times/0.3$ numerical aperture (NA) objectives to a silver-coated mirror at the reference beam and the hard biological tissues at the sample beam. The hard tissues are put on a piezoelectric transducer stage (PI, E-710.3CD, P-563.3CD) that moves vertically during axial scanning. The reflected light and back-scattering light of the two beams are combined by the same beam splitter to a tube lens and lens 2, and finally imaged on a two-dimensional camera (Silicon Imaging, SI-1300-M-CL). Lens 2 is used to adjust the magnification.

In our system, the visible-light waveband is chosen because we only need to acquire the surface configuration of the hard tissue. Therefore, it is not necessary to consider the penetration depth into the hard tissue and the visible-light facilitates the operation compared with the infrared light. Because of the response of the optical elements and the camera, a 250-nm bandwidth (FWHM) centered at 650 nm is used for this system, corresponding to $\sim 0.8 \mu\text{m}$ axial resolution theoretically. The axial resolution is measured using a mirror as a sample and scanning the piezoelectric transducer stage in the axial direction with a step size of $0.05 \mu\text{m}$. At the same time, the mirror in the reference beam

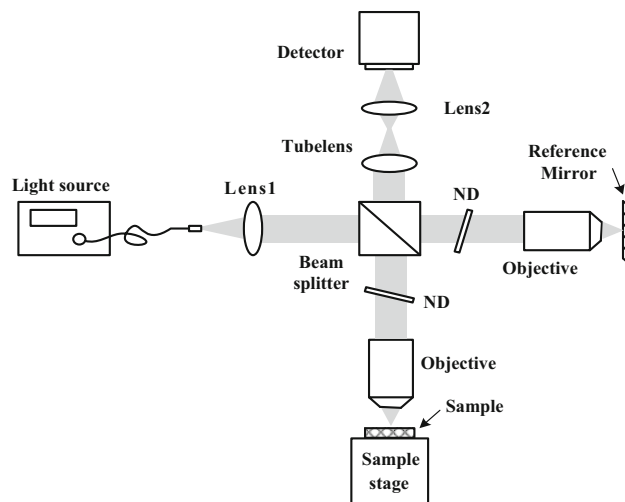


Fig. 1 The schematic diagram of the full-field OCM system

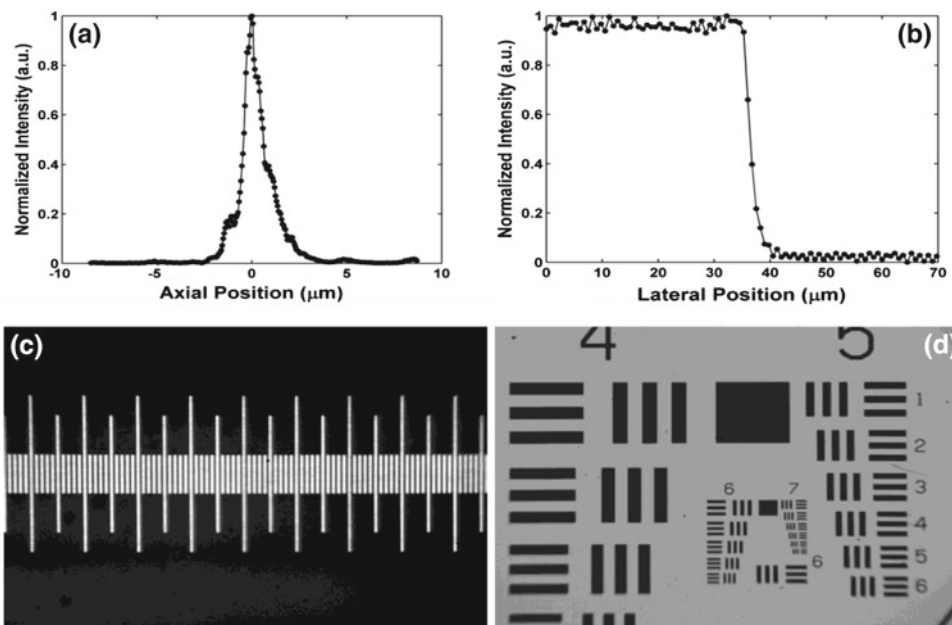
is kept static. The measured axial resolution is $1.1 \mu\text{m}$ as shown in Fig. 2a. However, to reduce the imaging time, we choose the step size of the scanning as $2 \mu\text{m}$, and the actual axial resolution is thus $2 \mu\text{m}$ when measuring the craters in hard tissues. The camera is a progressive-scan digital camera, with $1,280 \times 1,024$ pixels and $5.2 \mu\text{m}$ pitch, and the frame rate is ~ 25 frames/s. Taking into account the scanning time and reconstruction time, 4 s is required to obtain an en-face image. Comprehensively considering the field of view, the NA of the objective, magnification, and pixel pitch, the final lateral resolution is $3 \mu\text{m}$ as shown in Fig. 2b, which is obtained by measuring the sharp edge of the 1951 USAF glass slide resolution target. Adjusting the magnification by moving the position of lens 2, the field of view of the system can reach $\sim 1.1 \text{mm}$. For this measurement, the field of view is $900 \mu\text{m} \times 720 \mu\text{m}$ as shown in Fig. 2c. The 1951 USAF glass slide resolution target is also imaged by the system, with the elements of groups 5, 6, and 7, and part of group 4 being clearly imaged (Fig. 2d).

3 Experimental results

3.1 Dynamic evolutions of vaporization bubbles (VBs) and AP induced by a single laser pulse

Insets I, II, III, and IV in Fig. 3 are the captured VB pictures with the maximal volume V_{vbm} induced by 800, 600, 400, and $200 \mu\text{m}$ fibers transmitting 450/300 μs [full width at half-maximum (FWHM)] holmium laser pulses with 220, 300, 240, and 22 mJ energy in the free water region correspondingly. Under the same condition, the differently sequent images of AP (a), (b), (c), and (d) are presented, respectively. The hard tissues are bile stone or urinary

Fig. 2 **a** The measured axial resolution is 1.1 μm . **b** The measured lateral resolution is 3 μm . **c** The field of view of the system is 900 μm in the horizontal direction and 720 μm in the vertical direction. **d** The imaging of the 1951 USAF glass slide resolution target



calculus consisting of calcium oxalate monohydrate (COM) and uric acid (UC) components. In Fig. 3a, due to the uneven tissue surface, the left part of the free space between fiber end and tissue surface is bigger than that of the right. Consequently, the volume of the left AP is bigger than that of the right AP. The maximal AP consisting of vapor and bile stone debris occurs at 224 μs (see arrow). On the contrary, for Fig. 3b, the volume of the right AP is bigger than that of the left AP. The maximal AP consisting of vapor and calculus debris occurs at 232 μs (see arrow). After that time, it starts shrinking and maintains a final size at 348 μs . In Fig. 3c, although the fiber end is placed perpendicularly in contact with the calculus surface, little water still exists. The first and second maximal APs reach at 168 and 360 μs (see arrow), which consist of only vapor, the mixture of vapor and calculus debris, respectively. In Fig. 3d, three times the maximal AP occur at 80, 200, and 334 μs , respectively, which are all mixtures of vapor and calculus debris. The judgment criterion is whether or not there are still ablations debris existing after maximal AP. During these experiments, the high-speed camera (FAST-CAM SA1.1, Japan) is set at a speed rate of 500,000 frames per second with spatial resolution of 256 pixels \times 16 pixels.

3.2 Crater morphologies induced by laser pulses under various environments

To study the role of water environment during the laser ablation process, 2D and 3D scanning images for bile stone and urinary calculus craters, irradiated perpendicularly in air or in water by different core diameter fibers-guided holmium lasers with different parameters, are displayed in

Figs. 4, 5, 6 and 7 by using OCM, respectively. Holmium lasers of 450 μs , 84 mJ, 1 Hz; 300 μs , 300 mJ, 1 Hz; 300 μs , 240 mJ, 1 Hz, and 300 μs , 22 mJ, 1 Hz are transmitted in 800, 600, 400, and 200 μm fibers, respectively. For all experiments, these fibers are placed vertically in contact with tissue surfaces underwater. Except that the tissue samples for underwater experiments in Fig. 6 are urinary calculus consisting of calcium hydrogen phosphate dihydrate (CHPD) and those in Fig. 4 are bile stone, other samples are all urinary calculus (COM and UC). The pictures in Figs. 4 and 7 are obtained by scanning from XY and XZ directions, respectively. While the pictures in Figs. 5 and 6 are obtained by scanning from YZ and XYZ directions, respectively. All cross-sectional profiles that are at the deepest position of the craters are displayed. The heights and widths of ablation craters shown in Table 1 are averaged plus errors from five groups of samples under the same condition. It is assumed that the ablation efficiency is equal to the ratio of ablation height and pulse number and the average efficiency is their average value. Table 1 indicates the following when the distance between the fiber end and the tissue surface is unchangeable: (1) The heights of craters increase with the increase in the number of pulses both in water and in air (except in the two groups of data shown by “superscript a” in Table 1). (2) The surface diameters (widths) of the craters are smaller than the fiber core diameters except for multiple-pulse irradiation because of the relative position shifting between the fiber end and tissue surface induced by the recoil force. The craters induced in air have smaller depths and widths than those in water under the same condition. Ablations in air produce relatively rough and

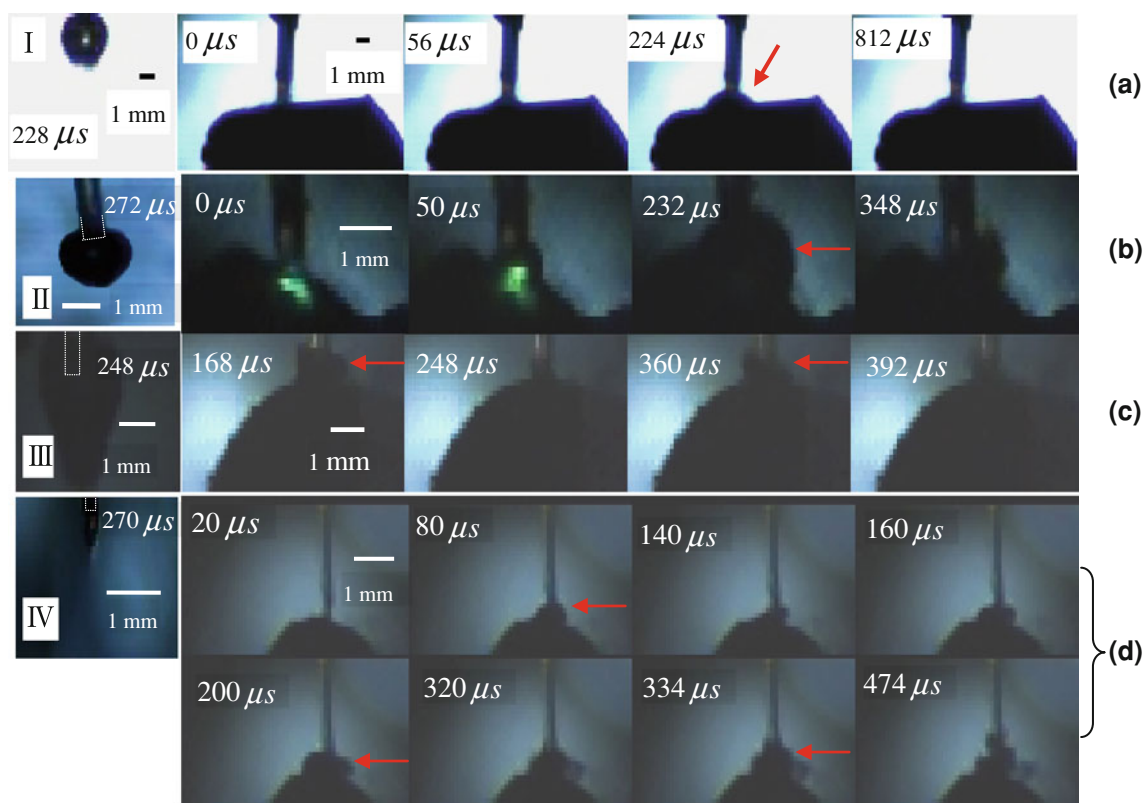


Fig. 3 Sequent images of ablation plumes with different core diameter fibers, pulse energies, and pulse durations. **a** 800 μm , 220 mJ, and 450 μs ; **b** 600 μm , 300 mJ, and 300 μs ; **c** 400 μm , 240 mJ, and 300 μs ; **d** 200 μm , 22 mJ, and 300 μs ; The hard tissues are the urinary calculus consisting of calcium oxalate monohydrate

(COM) and uric acid (UC) components for **b–d**, and are bile stones for **a**. Insets I, II III and IV are the VB pictures with maximal volume captured in the free water region. The given times are relative to the start of laser pulses

irregular contours and some protrusions along the rim of the craters (see red arrows in Fig. 5). (3) For the same laser parameters, the difference in ablation performance between that in air and in water for one laser pulse is not obvious, but the latter is slightly better than the former. (4) With the laser number further increasing, the ablation performance in water becomes significantly better than that in air, which mainly embodies bigger ablation volume, deeper crater height, more lubricious crater rim, etc. Moreover, in Fig. 5, crater depths induced by six and ten pulses in air have no obvious difference, but it is opposite in water because crater heights induced by five and ten pulses are all further increased. The main reasons are that the enhancement of energy conversion efficiency is further accumulated and VE is much more significant than ever. (5) The crater volumes induced by pulse lasers are always smaller than V_{vbm} . For example, for the 600 μm fiber, the crater volume [10 pulses ablation in water, w (width) = 741 μm , h (height) = 382 μm in Fig. 5] is confirmed to be smaller than V_{vbm} in Fig. 3, II ($h = 1,914 \mu\text{m}$, $w = 2,046 \mu\text{m}$). (6) Under the same parameters, the ablation efficiency will decrease with the increase in the number of laser pulses,

but the average ablation efficiency in water is higher than that in air, correspondingly. For example, for ablation efficiency in air and in water in Fig. 5, according to Table 1, $84.5 > 35 > 21.4$ and $85 > 59.5 > 38.6$; Furthermore, for average ablation efficiency, $47 < 61$. Note that for 400 μm fiber, the average ablation efficiency of 114 $\mu\text{m}/\text{number}$ in air is bigger than that of 66 $\mu\text{m}/\text{number}$ in water because the tensile coefficient of urinary calculus (COM and UC) is smaller than that of urinary calculus (CHPD). (7) The smaller the fiber diameter, the better will be the whole ablation performance (WAP). In order to objectively evaluate WAP of holmium lasers with different energies and transmission in different diameter fibers, we can assume WAP to be the ratio of average efficiency (AE) and the radiant energy density (ED). For 200, 400, and 600 μm fiber-guided laser ablation of urinary calculus (COM and UC) in air, $\text{ED}_1 = 70 \text{ J}/\text{cm}^2$, $\text{ED}_2 = 190 \text{ J}/\text{cm}^2$, $\text{ED}_3 = 106 \text{ J}/\text{cm}^2$, and $\text{AE}_1 = 87.4 \mu\text{m}/\text{number}$, $\text{AE}_2 = 114 \mu\text{m}/\text{number}$, and $\text{AE}_3 = 47 \mu\text{m}/\text{number}$, respectively. It is very easy to calculate that $\text{WAP}_1(1.25 \times 10^{-4} \text{ cm}^3/\text{number J}) > \text{WAP}_2(0.6 \times 10^{-4} \text{ cm}^3/\text{number J}) > \text{WAP}_3(0.44 \times 10^{-4} \text{ cm}^3/\text{number J})$.

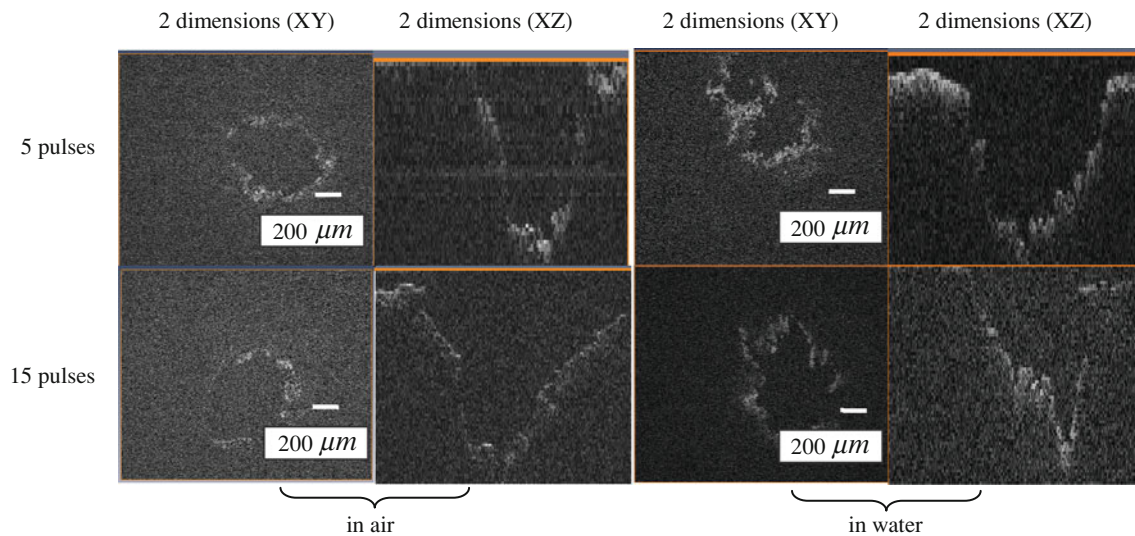


Fig. 4 Cross-sectional topography of fiber-guided holmium laser (450 μ s, 84 mJ, 1 Hz) pulses-induced craters in air and in water acquired with the OCM system. The 800 μ m fiber is in vertical touch with bile stone surfaces

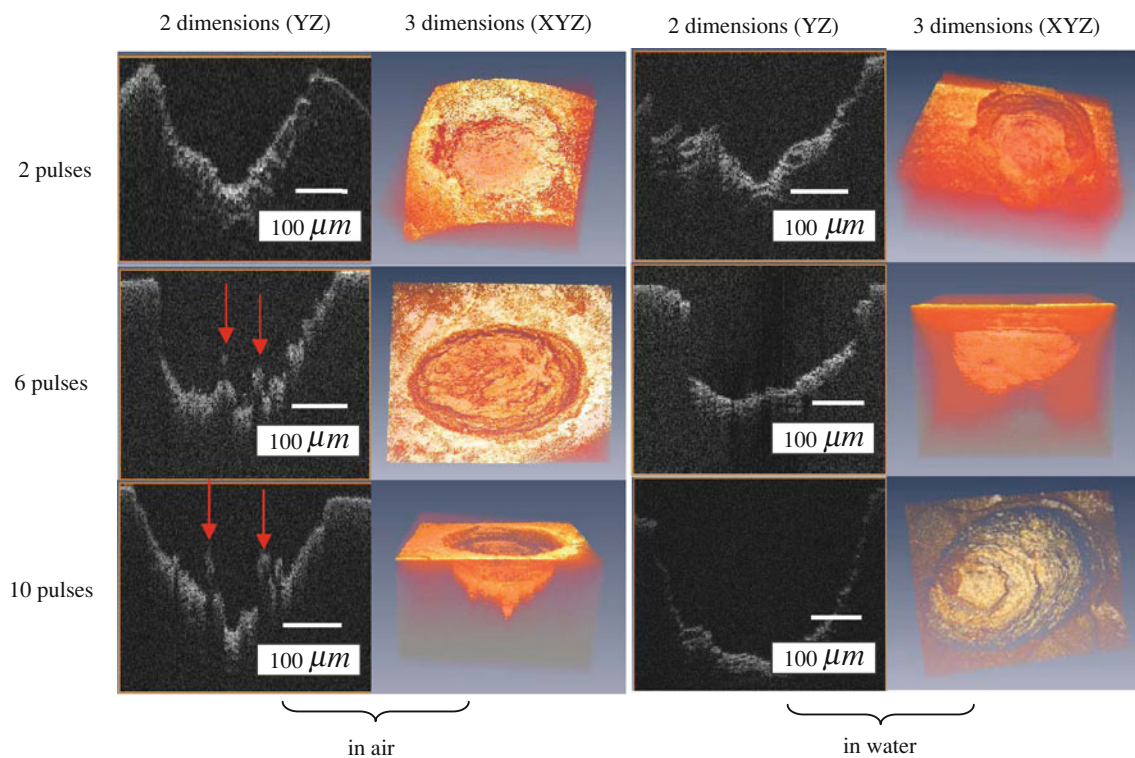


Fig. 5 Cross-sectional topography of fiber-guided holmium laser (300 μ s, 300 mJ, 1 Hz) pulses-induced craters in air and in water acquired with the OCM system. The 600 μ m fiber is in vertical touch with the urinary calculus (COM and UC) surfaces

4 Discussion

Only when laser fluence exceeds ablation threshold tissues may be ablated. Otherwise, the whole pulse energy is completely consumed during the process of VE. When the fiber end contacts the hard tissue perpendicularly, the spatial distribution of volumetric energy density with a

Gaussian temporal profile generates significant thermo-elastic transients [20]. These gradient transients are the driving force for all laser ablation processes that are not photochemically mediated [15, 20]. When they are beyond the maximal surface tension of tissue, material expulsion will occur and a crater will form immediately, accompanying a recoil to the tissue because of the law of

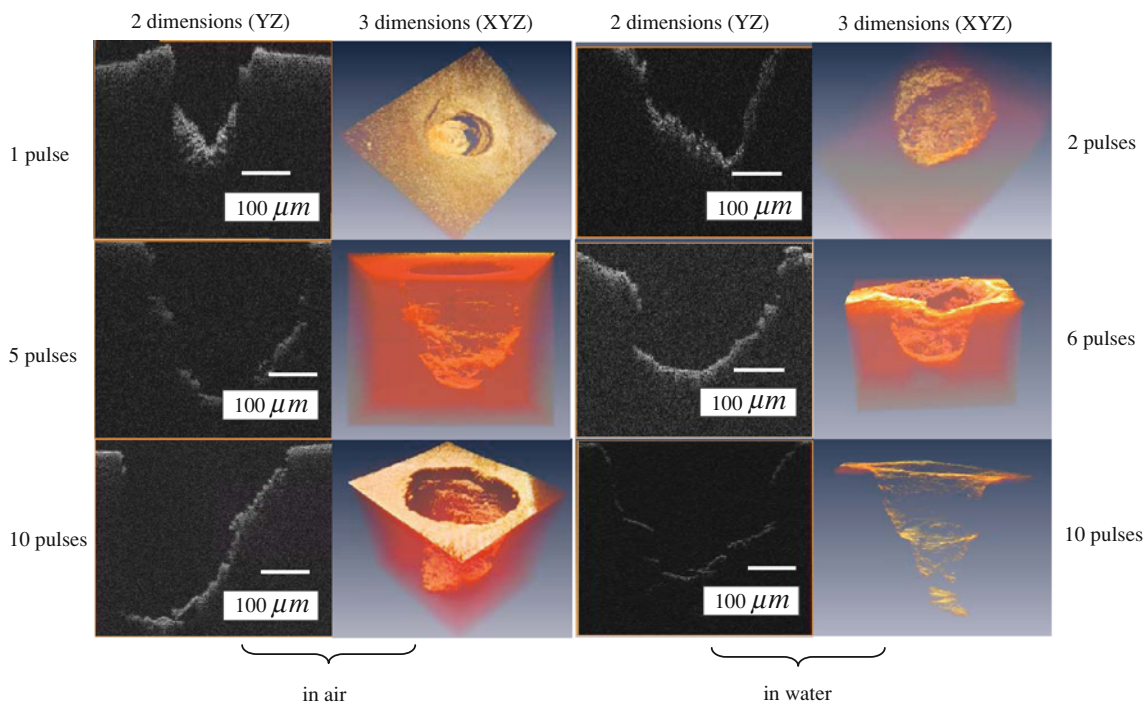


Fig. 6 Cross-sectional topography of fiber-guided holmium laser (300 μ s, 240 mJ, 1 Hz) pulses-induced craters in air and in water acquired with OCM system. The 400 μ m fiber is in vertical touch

with the urinary calculus surfaces. The components of calculus ablated in air are COM and UC, and the component in water is CHPD

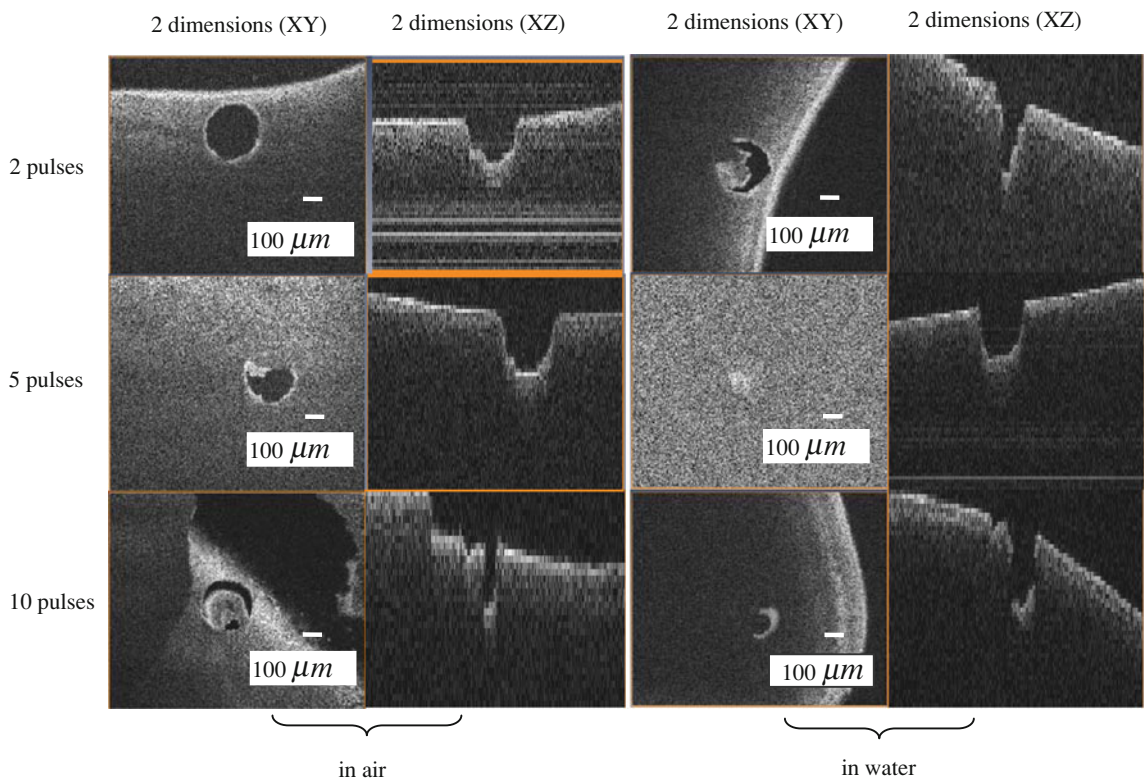


Fig. 7 Cross-sectional topography of fiber-guided holmium laser (300 μ s, 22 mJ, 1 Hz) pulses-induced craters in air and in water acquired with the OCM system. The 200 μ m fiber is in vertical touch

with the urinary calculus surfaces. Ablation by ten pulses, especially in air, indicates that obvious collapse occurs in the surrounding ablation region

Table 1 Parameters of the craters irradiated by fiber-guided holmium laser pulses

| Condition | 200 μm fiber (300 μs , 22 mJ, 1 Hz) | | | | | 400 μm fiber (300 μs , 240 mJ, 1 Hz) | | | | |
|-----------|--|-------------------------|---------------------------|-------|------|--|-------------------------|--------------------------|-------|-------|
| | NP | Width (μm) | Height (μm) | E | AE | NP | Width (μm) | Height (μm) | E | AE |
| In air | 2 | 278 \pm 18 | 234 \pm 18 | 117 | – | 1 | 255 \pm 7 | 150 \pm 10 | 150 | – |
| | 5 | 258 \pm 96 | 289 \pm 2 | 57.8 | 87.4 | 5 | 395 \pm 22 | 574 \pm 2 | 114.8 | 114 |
| | 10 | 71 \pm 4 | 271 \pm 18 ^a | / | – | 10 | 411 \pm 20 | 770 \pm 12 | 77 | – |
| In water | 2 | 222 \pm 74 | 363 \pm 2 | 181.5 | – | 2 | 375 \pm 18 | 147 \pm 5 | 73.5 | – |
| | 5 | 241 \pm 18 | 289 \pm 2 ^a | / | 111 | 5 | 410 \pm 17 | 384 \pm 2 | 64 | 66 |
| | 10 | 204 \pm 45 | 404 \pm 3 | 40.4 | – | 10 | 477 \pm 12 | 616 \pm 10 | 61 | – |
| Condition | 600 μm fiber (300 μs , 300 mJ, 1 Hz) | | | | | 800 μm fiber (450 μs , 84 mJ, 1 Hz) | | | | |
| | NP | Width (μm) | Height (μm) | E | AE | NP | Width (μm) | Height (μm) | E | AE |
| In air | 2 | 488 \pm 37 | 169 \pm 2 | 84.5 | – | / | / | / | / | / |
| | 6 | 495 \pm 5 | 209 \pm 6 | 35 | 47 | 5 | 868 \pm 57 | 1,286 \pm 29 | 257 | 173.7 |
| | 10 | 575 \pm 5 | 214 \pm 4 | 21.4 | – | 15 | 1,154 \pm 171 | 1,357 \pm 15 | 90.5 | – |
| | 2 | 549 \pm 1 | 170 \pm 5 | 85 | – | / | / | / | / | – |
| In water | 5 | 580 \pm 18 | 279 \pm 16 | 59.5 | 61 | 5 | 1,063 \pm 29 | 1,343 \pm 29 | 269 | 181 |
| | 10 | 666 \pm 75 | 386 \pm 4 | 38.6 | – | 15 | 1,234 \pm 151 | 1,380 \pm 30 | 92 | – |

NP number of pulses, E efficiency, the ratio of ablation height and pulse number, AE average efficiency

^a Indicates the unreasonable data

momentum conservation. The water beside the fiber end will flow into the crater along its brim. Because the confinement of the crater and fiber end, the water in crater will happen explosive vaporization induced by the rest of one laser, from which the force will impart crater brim intensively and can contribute to further ablate [14]. Simultaneously, the water flowing with high-speed in the crater acts on the rough contours of the crater, which will eject toward the outer side of the crater. Consequently, the crater surface will be slippery. Therefore, we may not agree with Altshuler's opinion [21] that solid particles of ablated material were accelerated against the walls of the crater, resulting in a polishing effect that removed debris and any protruding sharp edges. The tissues along the crater brim become molten layers immediately [22] and subsequently eject induced by the other part of one laser. Instantly, the crater cavity may become a vacuum cavity. With the pressures inside and outside the crater reaching equilibrium again, the water reenters the crater and the next explosive vaporization will occur again. The crater surface is polished by the so-called hydrodynamic piston effect until the laser end. Figure 3c, d indicates that the diameters of fibers directly influence the oscillation times (two times and three times, respectively) of AP underwater, which can support and prove the multi-times oscillation of AP for a single laser ablation underwater. Furthermore, our research results are not in agreement with Vogel's conclusion [15] that once the radiation is delivered to the tissue, the kinetics of the phase translations in the liquid environment are similar to those at

a tissue surface in a gaseous environment, except that surface vaporization plays no role. Since the crater volume is less than V_{vbm} , the force resulting from explosive vaporization contributes to the ablation significantly. The heat exchange coefficient of water is smaller than that of air [15], so there is a more effective transduction of the laser energy into thermomechanical energy underwater. For a small crater volume induced by part of or whole of a single pulse laser, the VE is not prominent and the ablation performance in water and in air are comparable. For multiple-pulses ablation, the crater volumes are large, so VE enhances and ablation efficiency improves. When the crater volumes come close to V_{vbm} , the flow speed of ejected water becomes slow and the ablation efficiency will decrease. We can deduce no ablation when the laser number increases to some value because the pressure waves resulting from VB collapses decrease inversely proportional to the transmitting distance and finally the force cannot exceed the maximal surface tension of tissue [23].

5 Conclusions

In conclusion, under the same laser parameters and tissues, the ablation performances in air and in water are comparable for a single laser. With the increase in the number of lasers, the crater volumes become bigger and the ablation performances in water become better than those in air because VE starts playing a positive role during the

ablation process. However, when the crater volume comes close to V_{vbm} , the effect of VE starts weakening. Compared with ablation in air, more pulses are required for ablation in water until no ablation. However, after only several pulses, the ablation efficiency in air starts decreasing acutely and even tends to zero. Moreover, the liquid volume between fiber end and tissue surface influences significantly the dynamics of AP. OCM is an effective tool with axial resolution of up to 1.1 μm for morphological measurements, which can help us to observe the fine structure and small variation of craters.

Acknowledgments This work is supported by the National Natural Science Foundation of China (Grant No. 61008054), the Special Fund for Basic Scientific Research of Central Colleges, China University of Geosciences (Wuhan) (CUG110408, CUG090112), and the program for Wuhan City Youth Chenguang Technology (Grant No. 201271031430). The authors appreciate Professor Ling Fu and Professor Zhengjia Li for their support with the experiments.

References

1. W.D. Song, M.H. Hong, B. Lukyanchuk, T.C. Chong, *J. Appl. Phys.* **95**, 2952 (2004)
2. C. Ohl, M. Arora, R. Dijkink, V. Janve, D. Lohse, *Appl. Phys. Lett.* **89**, 074102 (2006)
3. T.J. Dunbar, C. Cetinkaya, *Appl. Phys. Lett.* **91**, 051912 (2007)
4. J. Ren, M. Kelly, L. Hesselink, *Opt. Lett.* **30**, 1740 (2005)
5. S. Zhu, Y.F. Lu, M.H. Hong, X.Y. Chen, *J. Appl. Phys.* **89**, 2400 (2001)
6. S. Zhu, Y.F. Lu, M.H. Hong, *Appl. Phys. Lett.* **79**, 1396 (2001)
7. H.W. Kang, J. Oh, A.J. Welch, *Phys. Med. Biol.* **53**, 3381 (2008)
8. H.W. Kang, I. Rizoïu, A.J. Welch, *Phys. Med. Biol.* **52**, 7243 (2007)
9. D. Fried, N. Ashouri, T. Breunig, R. Shori, *Lasers Surg. Med.* **31**, 186 (2002)
10. T. Lü, Q. Xiao, D.Q. Xia, K. Ruan, Z.J. Li, *J. Biomed. Opt.* **15**, 048002 (2010)
11. H.W. Kang, A.J. Welch, *J. Appl. Phys.* **101**, 083101 (2007)
12. T. Sha, B. Wu, Y. Zhou, Y.B. Gao, *J. Appl. Phys.* **106**, 123507 (2009)
13. H.W. Kang, H. Lee, A.J. Welch, *J. Appl. Phys.* **103**, 083101 (2008)
14. T. Lü, Q. Xiao, Z.J. Li, *Appl. Opt.* **51**, 2505 (2012)
15. A. Vogel, V. Venugopalan, *Chem. Rev.* **103**, 577 (2003)
16. Q. Xiao, T. Lü, Z. Li, L. Fu, *Lasers Phys.* **21**, 1838 (2011)
17. Y. Kima, E.S. Choia, W. Kwaka, Y. Shina, W. Jungb, Y.-C. Ahnb, Z. Chen, *Opt. Laser Technol.* **40**, 625 (2008)
18. C.O. Mahony, M. Hill, M. Brunet, R. Duane, A. Mathewson, *Meas. Sci. Technol.* **14**, 1807 (2003)
19. C.E. Mercer, P. Anderson, G. Davis, *Int. Congr. Ser.* **1248**, 131 (2003)
20. A.D. Zweig, *J. Appl. Phys.* **70**, 1684 (1991)
21. G.B. Altshuler, A.V. Belikov, Y.A. Sinelnik, *Laser. Surg. Med.* **28**, 435 (2001)
22. M. Frenz, V. Romano, A.D. Zweig, H.P. Weber, *J. Appl. Phys.* **66**, 4496 (1989)
23. T. Lü, Z.J. Li, *Chin. Sci. Bull.* **56**, 1226 (2011)